




Nanofiber-reinforced soft fluidic micro-actuators

N R Sinatra^{1,2,4}, T Ranzani^{1,2,3}, J J Vlassak¹, K K Parker^{1,2}
and R J Wood^{1,2}

¹ John A. Paulson School of Engineering and Applied Sciences, Harvard University, Cambridge, MA, 02138, United States of America

² Wyss Institute for Biologically Inspired Engineering, Harvard University, Boston, MA, 02115, United States of America

E-mail: nsinatra@fas.harvard.edu

Received 31 August 2017, revised 2 February 2018

Accepted for publication 2 March 2018


Published 21 May 2018



Abstract

Soft pneumatic actuators are promising candidates for micro-manipulation and delicate gripping due to their wide range of motion and ease of fabrication. While existing elastomer-based devices have attracted attention due to their compliant structures, there is a need for materials that combine flexibility, controllable actuation, and robustness. This paper bridges this capability gap by introducing a novel fabrication strategy for nanofiber-reinforced soft micro-actuators. The design and manufacturing of composite PDMS/nanofiber actuators using soft lithography and rotary jet spinning is described. We examine the impact of lamina design and fiber orientation on actuator curvature, mechanical properties, and pressurization range. Composite actuators displayed a 25.8% higher maximum pressure than pure PDMS devices. Further, the best nanofiber-reinforced laminates tested were 2.3 times tougher than the control PDMS material while maintaining comparable elongation. Finally, bending and bending-twisting are demonstrated using pristine and laser-patterned nanofiber sheets, respectively.

Keywords: micro-actuators, nanofiber, pneumatic actuators, elastomers, composites, soft robotics

 Supplementary material for this article is available [online](#)

(Some figures may appear in colour only in the online journal)

1. Introduction

Over the past two decades, flexible fluidic actuators have gained prominence for their ability to conform to irregular shapes, deform with high curvature, exhibit smooth motions, interact with soft materials, and grasp micro-scale objects [1–5]. Soft pneumatic micro-scale actuators have recently been developed for use in minimally invasive surgery [6–9], tactile sensing [10], delicate gripping and micro-manipulation [11–13], and locomotion [1, 14]. Unlike conventional rigid devices, soft actuators facilitate gentle handling using elastomeric materials (e.g. polydimethylsiloxane) [4, 15] or

hydrogels [16]. Micro-scale soft actuators may be classified according to their expansion method, namely: membrane deflection (figure 1(a)), bellows expansion (figure 1(b)), balloon inflation (figure 1(c)), or contraction-based artificial muscles (figure 1(d)) [2]. Currently, state-of-the-art soft micro-actuators are fabricated using processes such as soft lithography, dip-coating, casting, and additive manufacturing [11, 13, 17, 18]. The bending modes of balloon-type micro-scale actuators manufactured through these methods are controlled by varying the air channel angle [19, 20], thickness or elastic modulus of layers surrounding the channel [9, 21–23], and device geometry [12, 13]. However, the curvature and full actuation pressure of elastomer-based micro-actuators are limited by the thickness of the strain limiting layer [17]. Reinforcing soft actuators with a strain limiting fiber has

³ Current affiliation: Mechanical Engineering Department, Boston University, Boston, MA, 02215, United States of America

⁴ Author to whom any correspondence should be addressed.

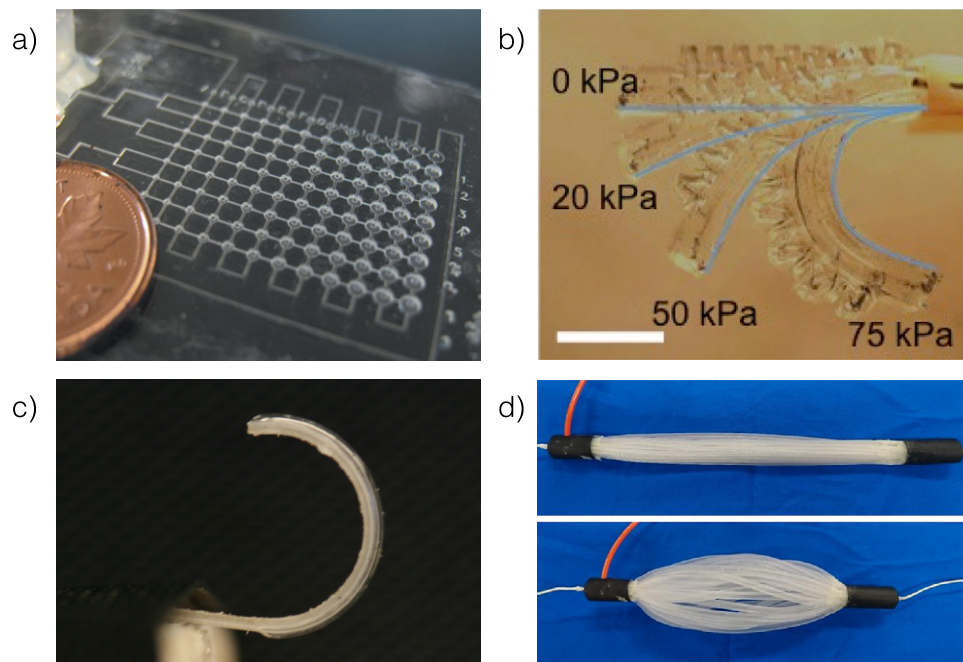


Figure 1. Classification of soft actuators. (a) Membrane deflection. Reproduced from [43] with permission of The Royal Society of Chemistry. (b) Bellows expansion. Scale bar: 1 mm. Reprinted from [11], Copyright 2015, with permission from Elsevier. (c) Balloon inflation. (d) Contraction-based artificial muscles. Reprinted from [27], Copyright 2017, with permission from Elsevier.

successfully bridged this capability gap for larger, centimeter-scale pneumatic actuators [24–27]. Fibers are an effective reinforcement layer for fluidic actuators because: (1) their inherent anisotropy facilitates directional control of actuator bending and mechanical properties, and (2) their flexibility and porosity are compatible with existing soft lithography techniques. However, yarn and woven fiber-based reinforcements used in macro-scale devices are too large to act as a strain limiting layer for micro-scale actuators. A lightweight, yet tough fibrous material is needed to regulate micro-scale bending without significantly increasing the actuator size, reducing compliance, or impairing its interaction with delicate objects.

Nanofibers are a promising reinforcement material for soft micro-actuators due to their flexibility, high specific strength, customizable size and mechanical properties, and ease of processing [28, 29]. Nonwoven nanofabrics have previously been established as a basis for a wide range of applications, including: tissue engineering scaffolds [30, 31], artificial muscles and bio-actuators [32, 33], filtration membranes [34, 35], flexible sensors [36, 37], and textiles [38]. Using fabrication processes such as rotary jet spinning and electrospinning, it is possible to regulate the mechanical and material properties of nanofabrics and to manufacture uniform fiber sheets with customizable fiber diameter and orientation [39–42]. Despite their compliance, robustness, and controllable morphology, nanofibers have not yet been integrated into soft robotic devices.

Here, we present a novel fabrication process that combines rotary jet spinning and soft lithography to manufacture nanofiber-reinforced pneumatic PDMS actuators. Incorporating a nanofibrous strain limiting layer increases toughness and modulates curvature without increasing the

overall thickness of the actuator. Moreover, by leveraging lithographic processes designed for microscale manufacturing, we can repeatedly construct soft actuators with $30\ \mu\text{m}$ feature sizes. Furthermore, we examine the influence of layer design and nanofiber orientation on actuator curvature, bulk mechanical properties, and actuation pressure. To gain additional insight into the system and to predict actuator curvature as a function of pneumatic pressure, a quasi-static analytical model is derived. Finally, we demonstrate the ability of this method to replicate two benchmark bending modes of macro-scale fiber reinforced actuators: bending and bending-twisting. Our data reveal that composite micro-scale actuators are tougher and stronger than pure elastomer designs, while displaying comparable elongation. We found that nanofiber-reinforced platforms exhibit lower curvature than PDMS-only devices, and that the analytical model predicts experimental trends for both categories of micro-actuators.

2. Experimental methods

2.1. Nanofiber fabrication using rotary jet spinning

Nonwoven nanofiber sheets were manufactured using rotary jet spinning, following a previously reported protocol [31, 39]. A solution of 3 wt./v% nylon-6 (Nylon 6, Sigma-Aldrich, St. Louis, MO) / 3 wt./v% polyurethane (McMaster Carr, Princeton, NJ) was prepared in 1,1,1,3,3,3-hexafluoro-2-propanol (HFIP, Sigma-Aldrich, St. Louis, MO), and infused into the reservoir for one minute at a rate of $5\ \text{ml}\ \text{min}^{-1}$ (figure 2(a)). The resulting nanofiber sheets were collected using a rotating cylindrical mandrel attached to a linear motor. Following fiber fabrication, samples were compressed to remove creases and to improve uniformity during the

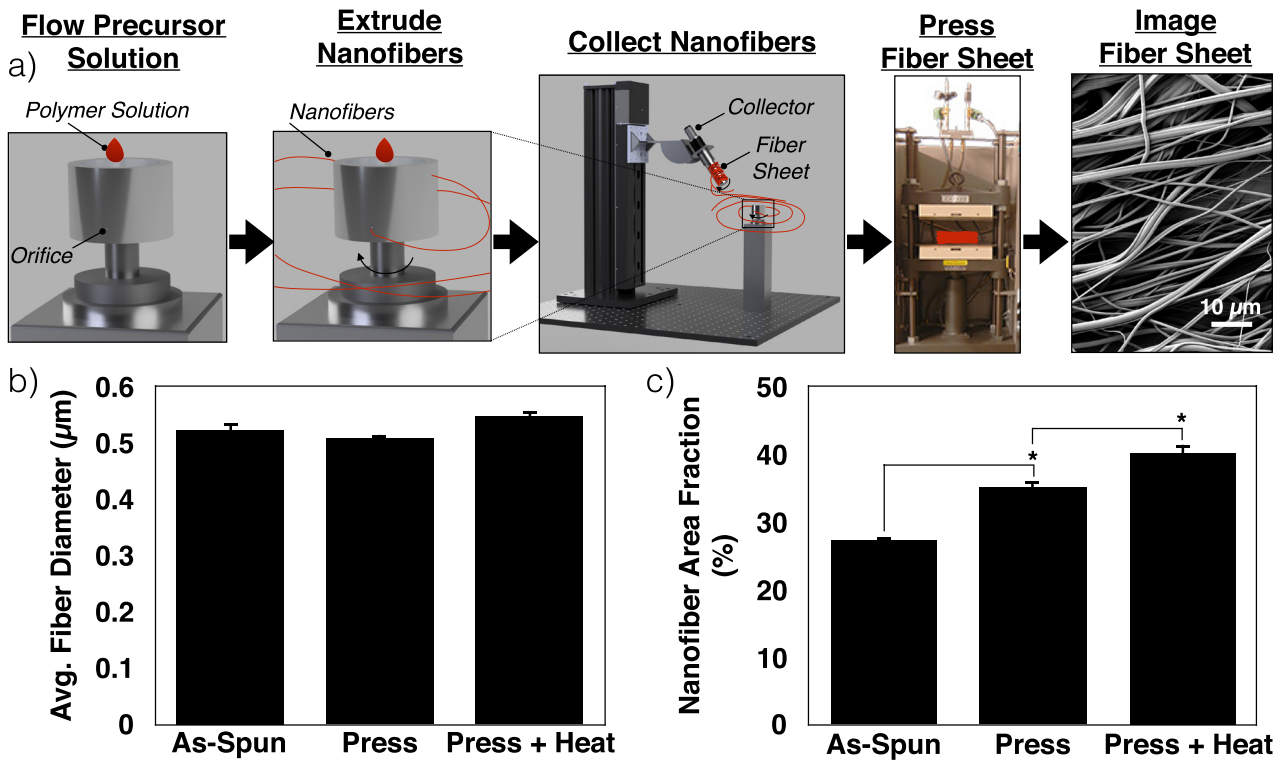


Figure 2. (a) Schematic of the fiber fabrication process using the rotary jet spinning system, post-processing using a hydraulic press [46], and a scanning electron micrograph of 6 wt./v% Nylon/Polyurethane (1:1) nanofibers, (b) average diameter and (c) porosity of as-spun, pressed, and pressed/heated nanofiber sheets. $n = 3$ production runs per condition, One sample/run, three random fields of view/sample. Error is reported as SEM. * indicates $p < 0.05$.

subsequent soft lithography process. Each sheet was pressed for 10 min at 3000 lbs (applied over an area of 132 cm²) and 50 °C using a laboratory hydraulic molding press (Carver Laboratory Press, Wabash, IN).

2.2. Actuator design and fabrication

Composite nanofiber micro-actuators were fabricated using a four step process. First, PDMS was formulated by combining Sylgard 184 (Dow Corning, MI, USA) elastomer base and curing agent in a 10:1 ratio. The mixture was spin coated onto an embossed silicon wafer at 300 rpm, de-gassed in an vacuum chamber for 10 min, thermally cured for two hours at 65 °C, and then removed from the wafer (figure 3(a)). Next, a PDMS layer was spin coated at 100rpm onto an unpatterned silicon wafer, de-gassed, and partially crosslinked for ten minutes at 75 °C. Using a film applicator, a nanofiber sheet was coated with 20 μm uncured PDMS. The fiber sheet was placed on the semi-cured PDMS wafer, spin coated at 200 rpm, thermally cured for 30 min, and removed from the wafer (figure 3(b)). At this stage, the soft lithography-based workflow can be easily adapted to construct other laminate configurations. In addition to the three-layer (air channel, passive PDMS layer, nanofiber layer) actuator, we fabricated a four-layer composite (air channel, passive PDMS layer, nanofiber layer, passive PDMS layer) to test the effect of the nanofiber layer position with respect to the neutral axis on actuator curvature. The four-layer laminate was fabricated by spin coating an additional layer of PDMS onto the nanofiber sheet before the 30 min

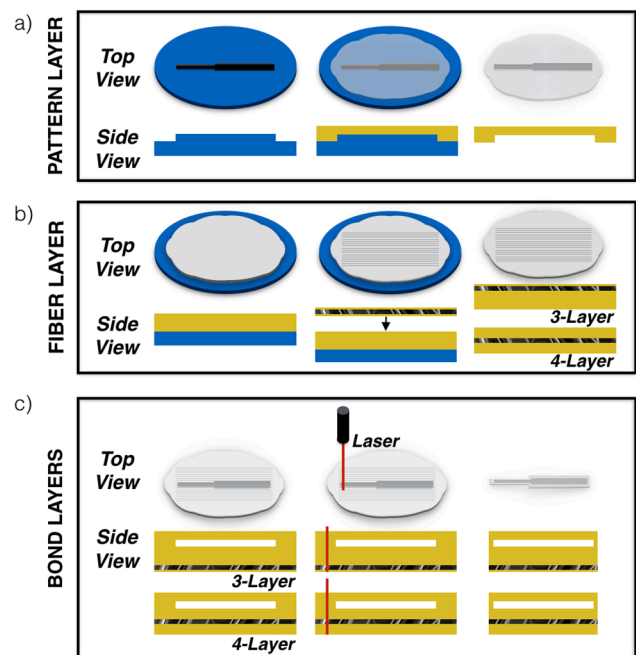


Figure 3. Fabricating composite soft actuators. (a) PDMS (yellow) is coated, cured, and peeled from a patterned wafer (blue). (b) PDMS and fiber (striped) layers are coated, cured, and removed from a blank wafer. (c) Sub-laminates are plasma bonded and the actuator is laser-cut.

cure stage. The fabrication process for three- and four-layer actuators was identical following this step: the patterned and unpatterned layers were irreversibly bonded together using

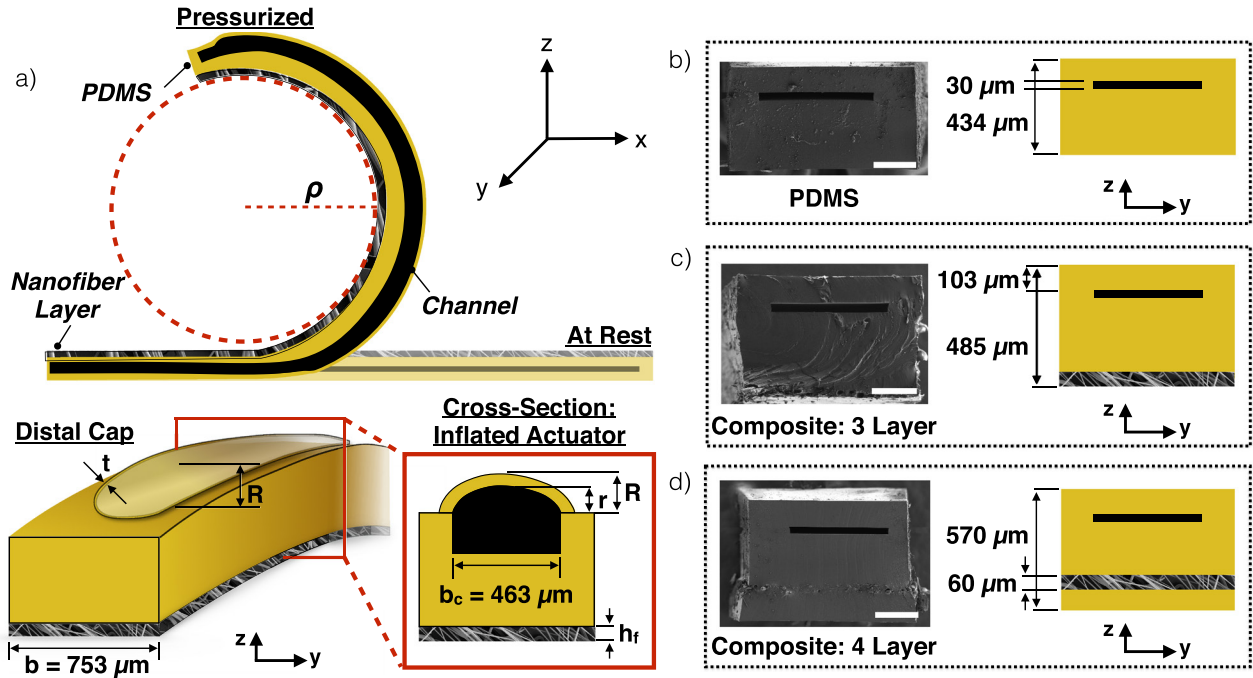


Figure 4. (a) Illustration of at-rest and inflated three-layer actuator. The left end of the actuator is fixed, while the distal end moves freely. Isotropic view and cross-sectional schematic of the distal tip of an inflated 3-layer composite actuator. Cross-sectional diagrams and scanning electron micrographs of (b) PDMS, (c) Three- and (d) four-layer laminates. Scale: $200 \mu\text{m}$.

an oxygen plasma treatment (65W for 30s). The resulting composite actuators were machined in the desired geometry using a custom DPSS laser, then removed from the bulk sheet (figure 3(c)). Lastly, catheter tubing (MicroRenathane Catheter Tubing, Braintree Scientific, Inc., MA, USA) was inserted and sealed (Scotch-Weld 1838 B/A, 3M) into the channel of each micro-actuator.

2.3. Modeling bending of composite soft actuators

An analytical 2D model was derived to better understand the effect of layer design and composition on bending behavior of multi-layer composite micro-actuators. Our model includes the following assumptions: (1) perfect bonding and no slippage between layers, (2) each layer is homogeneous, with known properties, (3) the PDMS matrix and membrane are incompressible, (4) the bending moment of a pressurized actuator is constant along the actuator length, (5) the Young's moduli of PDMS and polymer nanofibers remain constant during pressurization, (6) the strain limiting layer is inextensible, and (7) gravity is neglected during actuator bending.

Here, a pressurized micro-actuator was considered to be a clamped-free cantilever beam (figure 4(a)), and modeled as an incompressible Neo-Hookean material. The assumption of incompressibility yields the following invariant relationship between the three principal stretch ratios ($\lambda_1, \lambda_2, \lambda_3$):

$$\lambda_1 \lambda_2 \lambda_3 = 1. \quad (1)$$

The longitudinal stretch was represented by $\lambda_1 = \frac{dl}{dL}$, in which L indicates the initial length of the actuator and l is the length in the deformed state. Here, we set $\lambda_1 = 1$ under the assumption

that longitudinal deformation is negligible compared to axial and circumferential expansion. Thus, the circumferential (λ_2) and axial (λ_3) stretches can be related as $\lambda_3 = \frac{1}{\lambda_2}$. Further, circumferential stretch was defined as $\lambda_2 = \frac{s}{2a}$, where s denotes the arc length of the inflating air channel and $2a$ indicates the width of the inflated channel. Using geometry,

$$\lambda_2 = \frac{s}{2a} \quad (2)$$

$$= \frac{r\theta}{2a} \quad (3)$$

$$= \frac{r}{a} \arcsin \frac{a}{r}. \quad (4)$$

Here, r represents the radius of curvature of the circular sector. Next, the axial stretch was defined as $\lambda_3 = \frac{t}{T}$, in which T represents the thickness of the upper channel membrane prior to inflation (measured using scanning electron microscopy as 0.103 mm), and t is the thickness of the inflated air channel membrane. Using the incompressibility condition, we can express both λ_3 and t in terms of λ_2 :

$$\lambda_3 = \frac{t}{T} = \frac{1}{\lambda_2} \quad (5)$$

$$t = \lambda_3 T \quad (6)$$

$$= \frac{aT}{r \arcsin \frac{a}{r}}. \quad (7)$$

Therefore, only one independent stretch is present for this geometry. As the actuator inflates, the relationship between radius of curvature of the air channel membrane and input

pressure (P) was calculated by equating the hoop stress of a thin-walled cylindrical pressure vessel in terms of the applied pressure ($\sigma_2 = \frac{Pr}{t}$) and the principal stretch ratios ($\sigma_2 = \mu(\lambda_2^2 - \lambda_3^2)$):

$$P = \frac{\mu}{r} \frac{T}{\frac{r}{a} \arcsin \frac{a}{r}} \left(\left(\frac{r}{a} \arcsin \frac{a}{r} \right)^2 - \left(\frac{1}{\frac{r}{a} \arcsin \frac{a}{r}} \right)^2 \right). \quad (8)$$

In this expression, μ represents the shear modulus of the PDMS membrane. For the purposes of this analysis, we assume $E_m = 3\mu$ (where E_m is the membrane Young's modulus) to be constant throughout pressurization; however, future studies will reflect the instantaneous elastic modulus as the elastomeric membrane strains and stiffens. Although the inflating membrane is monolithic, the stiffness of PDMS samples undergoes a shift from bulk behavior to dimension dependence below a thickness of 200 μm . Below this inflection point, the Young's modulus of PDMS samples is greater than 1.2 MPa. [44] As the thickness of the inflating membrane is within this range, we assume $E_m = 1.2$ MPa for equation (8). However, the bulk elastic modulus (recorded as 0.6 MPa,) was used for calculations involving the thicker, passive PDMS layers in the actuator.

As per Euler–Bernoulli beam theory, the curvature ($\frac{1}{\rho}$) of a composite beam is given by:

$$\frac{1}{\rho} = \frac{M}{EI_i + E_m I_m} \quad (9)$$

where E is the effective Young's modulus of the composite beam, I_i is the total area moment of inertia for the passive PDMS and fiber lamina, E_m is the Young's modulus of the inflating PDMS membrane, I_m is the area moment of inertia of the membrane, and M is the bending torque of the actuator due to air pressure on the distal cap. The Young's moduli of 3 wt.% nylon / 3 wt.% polyurethane nanofiber sheets embedded longitudinally and transversely in 20 μm PDMS layers were measured to be 1.499 MPa and 0.741 MPa, respectively (supplementary figure 1(a) (stacks.iop.org/JMM/28/084002/mmedia)).

The area moment of inertia for the composite laminate structures can be calculated using a parallel axis theorem:

$$I = \sum_{i=1}^l (I_i + A_i d_i^2). \quad (10)$$

In this expression, I_i is the moment of inertia for an individual layer, A_i is the layer's cross-sectional area, and d_i is the distance from the layer's centroid to the actuator centroid. The summation index i represents each layer in the composite structure, and l is the total number of layers in a given actuator. The moment of inertia for rectangular layers of PDMS and nanofibers was calculated using the following equation:

$$I_i = \frac{b_i h_i^3}{12} + b_i h_i d_i^2 \quad (11)$$

in which b_i and h_i represent the width and height, respectively, of a given layer in a laminate. For composite laminates with disparate elastic moduli, the width of the stiffer layer is typically scaled using an expansion factor, $n = \frac{E_1}{E_2}$, in which

$E_2 < E_1$. Thus, the width of the nanofiber layer was determined by multiplying the expansion factor $n = \frac{E_{\text{fiber}}}{E_{\text{PDMS}}}$ by the measured width of the fiber lamina. The inflated air channel was considered to be a hollow circular sector, and its area moment of inertia was calculated as follows:

$$I_i = \frac{\alpha}{4} (R^4 - r^4) \left(1 - \frac{\sin \alpha \cos \alpha}{\alpha} \right). \quad (12)$$

In this equation, α is one half the circular sector angle, and R and r denote the outer and inner radii of curvature of the inflated channel, respectively (figure 4(a)) [45]. Thus, I_m was calculated using equations (10) and (12). Using equations (9)–(12), the moments of inertia of each layer were summed to determine the total moment of inertia for the composite actuator.

Finally, the bending torque of internal air pressure (M) was calculated. Based on assumption (4), the bending moment is constant along the longitudinal axis of the actuator. In this analysis, M was derived with respect to the cap (figure 4(a)) with which the air channel terminates at the distal end of the actuator. The bending torque of internal air pressure on the distal cap was determined by multiplying the applied air pressure (P), the summed cross-sectional areas of the inflated channel and the original area of the air channel (A_{in}), and the lever arm of the inflated area with respect to the total actuator centroid (d_{in}):

$$M = PA_{\text{in}} d_{\text{in}}. \quad (13)$$

We assume that the cross-sectional area of the inflated section is constant along the length of the actuator, and that the distance between the distal cap and the end of the actuator is negligibly small with respect to the total device length. Using this analytical framework, the actuator curvature was calculated as a function of pressure and compared with empirical results.

2.4. Nanofiber image analysis

Nanofiber samples were affixed to carbon-taped scanning electron microscopy stubs, and subsequently sputter coated using a Pt/Pd target (Denton Vacuum, Moorestown, NJ). Coated stubs were imaged using a field emission scanning electron microscope (Carl Zeiss, Dresden, Germany). Image analysis was performed using Fiji (<http://ji.sc/Fiji>, Ashburn, VA). For each case, 135 fibers were analyzed using three random fields of view per sample and three samples per condition.

2.5. Mechanical characterization of composite actuators

Rectangular samples of PDMS (length = 20 mm, width = 10 mm), monolithic nanofabrics coated in 20 μm PDMS (length = 20 mm, width = 10 mm), and composite PDMS–nanofiber laminates (length = 20 mm, width = 0.78 mm) were laser cut from bulk samples. For fibrous materials, 2 mm on either side of each sheet was sealed using epoxy and tape to prevent slippage of fibers in the Instron clamps. Using a uniaxial tensile test (Instron 5544A, Norwood, MA), specimens were extended in air at a rate of 8 mm min^{-1} until failure. Before each run, the gauge length, width, and thickness of

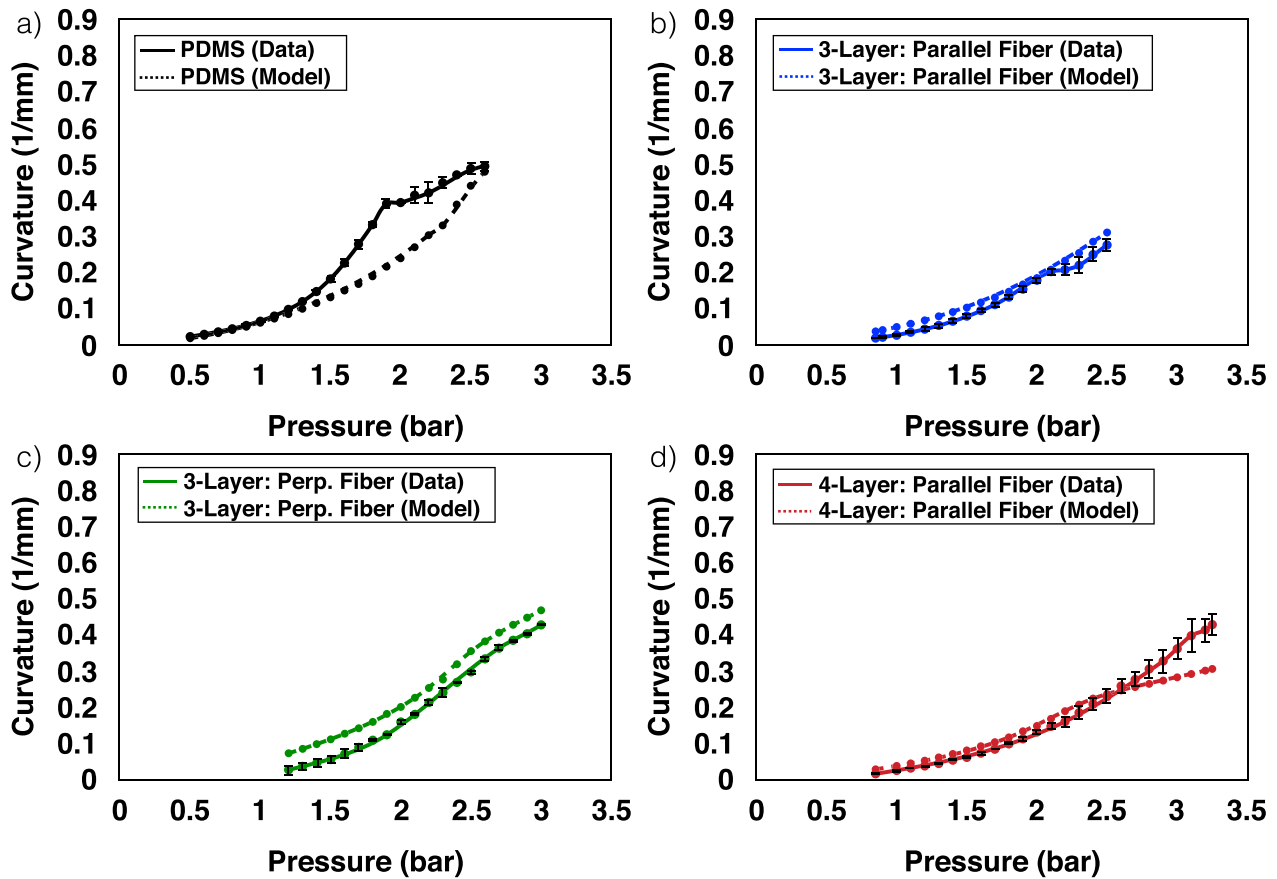


Figure 5. Analytical and experimental results for the curvature of (a) PDMS-only, (b) Three-layer composite device with nanofibers parallel to actuator, (c) Three-layer composite with nanofibers perpendicular to actuator, and (d) Four-layer composite with nanofibers parallel to actuator. $n = 2-3$ actuators per condition. All error is reported as SEM.

each sample were recorded using a micrometer. Following the measurement, materials were weighed; uniform density was assumed for each sample.

2.6. Actuator bending characterization

The curvature of composite micro-actuators was recorded in air. First, each actuator was fixed at a distance of 12 cm from a Canon Eos Rebel Ti. Next, the actuators were pressurized using a syringe pump at a rate of 1 ml min^{-1} until failure. Actuators were photographed every 0.1 bar; the resulting images were analyzed using Fiji.

3. Results and discussion

3.1. Nanofiber characterization

Prior to assembling the composite micro-actuators, we examined whether fiber post-processing steps (e.g. compression molding and heating) alter the fiber diameter or porosity of nanofiber networks. First, nanofiber sheets were manufactured via rotary jet spinning (figure 2(a)), as described in section 2.1. Average fiber diameter (figure 2(b)) and fabric porosity (reported in figure 2(c) as the fiber area fraction) were measured for as-spun nanofiber sheets, and compared to those of samples that had been pressed, and both pressed

and heated. Samples were heated for 30 min at 75° , to simulate the conditions under which PDMS is cured. While neither post-processing step significantly impacted the average fiber diameter, the area fraction of fibers increased after both pressing and heating. This result is logical, as the compression process reduces the area between adjacent nanofiber layers. The lack of damage to fiber sheets during post-processing confirms our capability to regulate fiber morphology during the nanofiber manufacturing processes, and the ability of nanofibers to withstand post-processing steps for soft lithography.

3.2. Effect of nanofiber orientation and actuator design on bending

Having established a consistent method to control nanofabric morphology, we then investigated whether the position of the nanofiber layer relative to the neutral axis impacts actuator curvature and pressurization range. Composite actuators were fabricated using a four step method, detailed in section 2.2 and illustrated in figure 3. This process was used to assemble three- and four-layer devices, varying the location of the nanofiber sheet. As a control, two-layer actuators (air channel, passive PDMS layer) were fabricated using only PDMS (figure 4(b)). Three-layer actuators featured the fiber sheet as the outer layer of the device (figure 4(c)), while four-layer actuators incorporated an additional PDMS layer around the nanotextiles

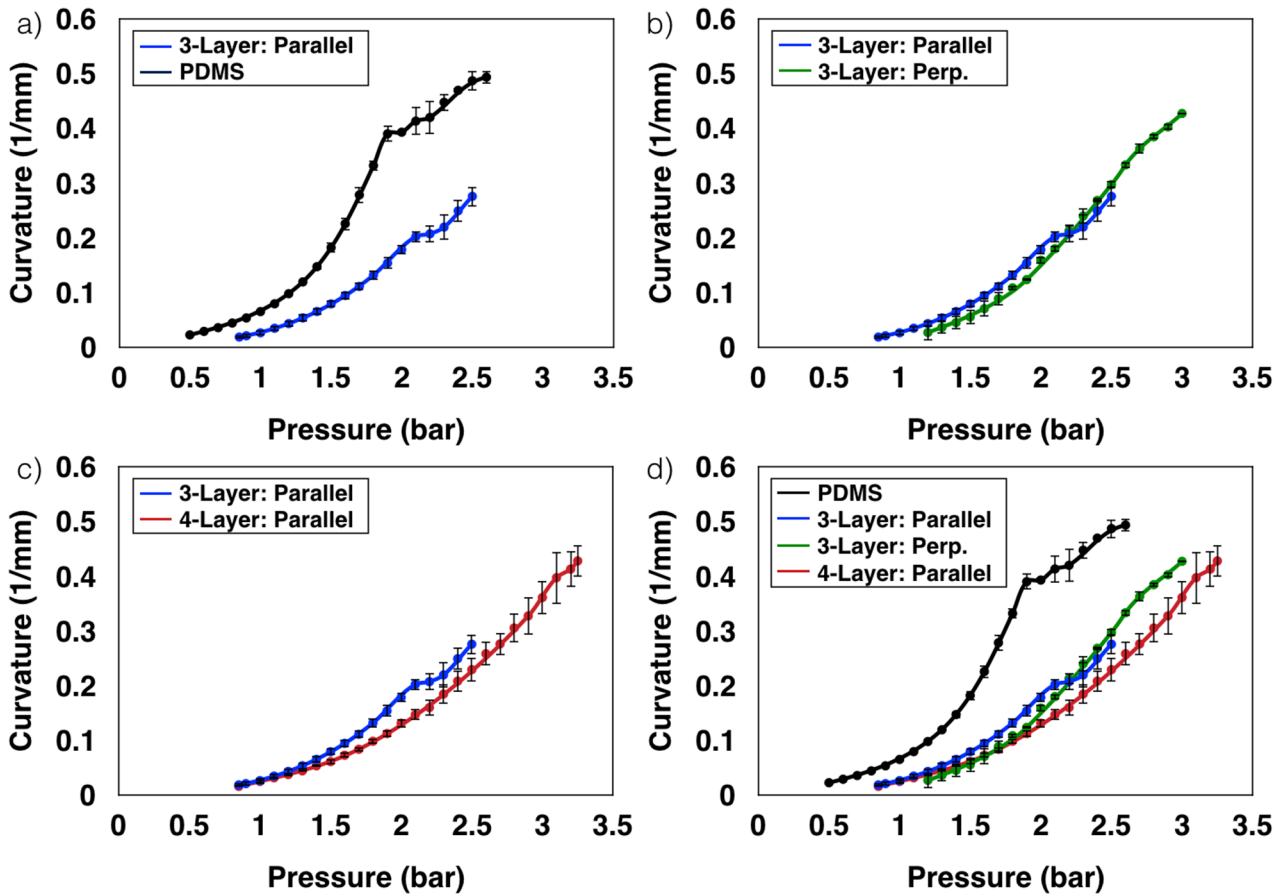


Figure 6. Curvature of (a) pure PDMS and three-Layer composite device with nanofibers parallel to actuator, (b) Three-Layer composite actuators with parallel and perpendicular fibers, (c) Three- and four-Layer PDMS-nanofiber actuators with fibers oriented parallel to device, and (d) Comparison of curvature for three- and four-layer composite and PDMS-only actuators. $n = 2-3$ actuators per condition. All error is reported as SEM.

(figure 4(d)). To understand the impact of fiber orientation on actuator bending, nanofiber sheets were positioned at either 0° or 90° relative to the longitudinal axis of three-layer actuators.

Using the analytical framework discussed in section 2.3, actuator curvature was modeled as a function of pressure and compared to empirical data. All actuators were pressurized from rest (0 bar) to failure. To ensure consistent statistical analysis among each sample set, averaged experimental values are shown for the range between the onset of inflation (constant within each device layout) and the earliest failure point within that category; analytical values are displayed within the same range for each actuator design (figure 5). Figure 5(a) displays theoretical and empirical results for the control two-layer actuators, composed only of PDMS. Nonlinearity in the relation between pressure and curvature is due to that of the pressure-stretch and pressure-area relations (supplementary figure 2), as well as the balance between membrane thinning and material stiffening during inflation [47, 48]. As the air channel is pressurized, curvature will first increase rapidly as the elastomeric membrane inflates and its thickness decreases; thinning of the inextensible membrane can be assumed according to assumption (3). At higher pressures, membrane thinning will outweigh the impact of the material stiffening, and the rate of change of the curvature will decrease before the membrane ruptures. Similar trends are evident for three-layer

composite actuators with nanofibers oriented parallel (figure 5(b)) and perpendicular (figure 5(c)) to the longitudinal axis, and four-layer actuators with parallel fibers (figure 5(d)). The analytical model addresses this nonlinearity by assuming the reference state of the actuator air channel to be inflated, and considering small perturbations from this deformed geometry. Generally, the model predicts the experimental trends well, though we expect that future analyses will increase the accuracy of analytical predictions by accounting for membrane stiffening during inflation (i.e. determining the instantaneous Young's modulus rather than assuming $E_m = 3\mu$).

Figure 6(a) compares the pressure-curvature relationship for PDMS-only and three-layer fiber-reinforced micro-actuators. Curvature is inversely proportional to actuator stiffness; thus, the fully elastomeric actuators are more sensitive than fibrous devices to pneumatic pressure and display greater curvature for a given pressure. However, this correlation does not apply between composite actuators with parallel (Young's modulus: 1.4992 MPa) and perpendicularly (Young's modulus: 0.741 MPa) oriented nanofibers. For both parallel and perpendicularly oriented nanofibers, the rate of change for actuator radius of curvature is inversely proportional to applied pressure (figure 6(b)). Experimentally, actuators with fibers oriented at 90° (labeled perpendicular) begin inflating at a slightly higher pressure, as compared to those with fibers

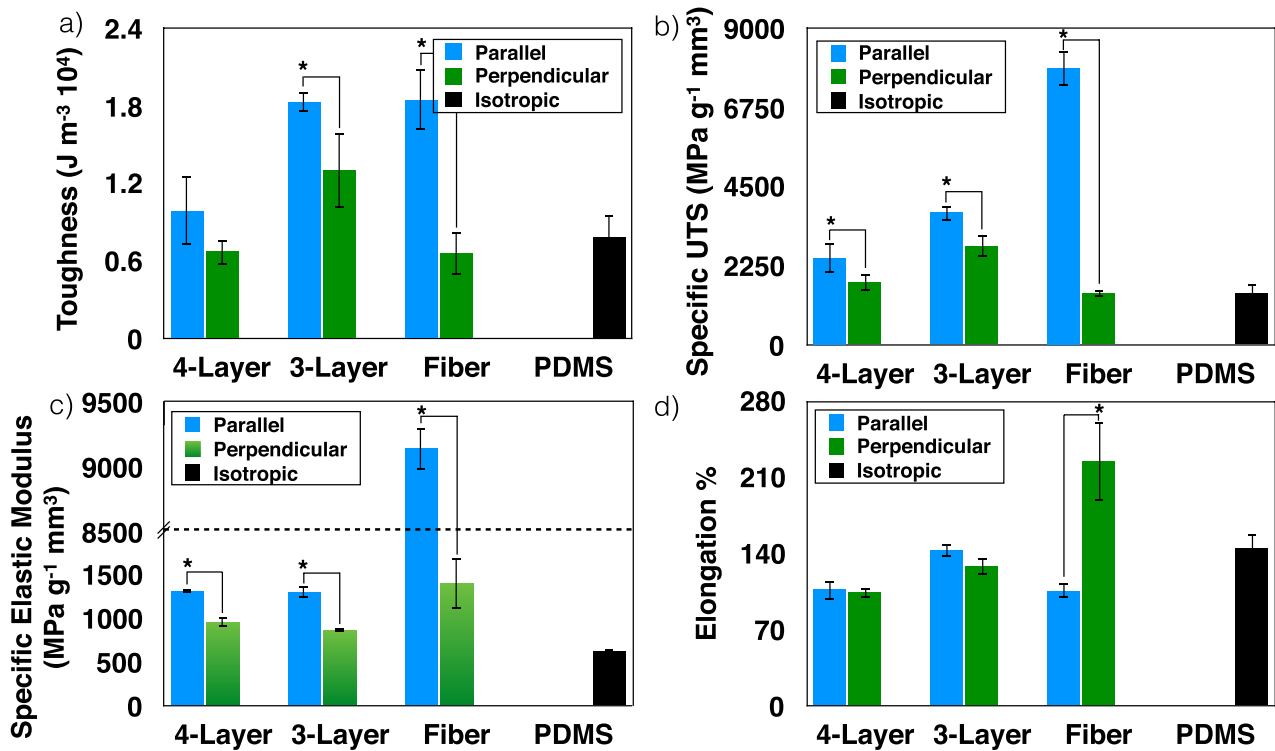


Figure 7. Mechanical properties of composite and elastomer actuators. (a) Toughness, (b) specific ultimate tensile strength (UTS), (c) specific elastic modulus, and (d) elongation of three- and four-layer composite actuators, nanofiber sheets embedded in a $20 \mu\text{m}$ PDMS layer, and pure PDMS actuators. $n = 3$ samples per condition. All error reported as SEM. * indicates $p < 0.05$.

placed at 0° (labeled parallel). Although the perpendicular nanofibers have a lower Young's modulus when encased in PDMS, it appears that the stiffer parallel fibers are more sensitive to applied pressure and experience more deflection for a given pressure. Decreasing stiffness of the strain limiting layer in the bend direction shifts the laminate's centroid upwards toward the inflating membrane, thus inhibiting bending at low pressures. Moreover, the orientation of nanofibers orthogonal to the air channel potentially stiffens the inflation chamber, limiting its ability to expand. While the analytical model presented here predicts this behavior, the deformation of the inflated channel due to directional stiffening may be explored in future studies using finite-element method modeling.

Empirical data for three- and four-layer actuators reinforced by parallel fibers is shown in figure 6(c). While both devices initiate bending at a similar pressure, three-layer devices display slightly higher curvature under moderate pressure, and four-layer actuators sustain significantly higher pressurization before failure. This result indicates that while movement of the neutral axis toward the air channel inhibits bending, positioning the fibrous layer within the actuator increases robustness of the device. Finally, figure 6(d) displays the pressure-curvature relations for all four actuator varieties.

Overall, all composite actuator designs displayed a significantly larger curvature compared to pure PDMS actuators. Moreover, composite designs were able to withstand up to 30% higher pressure before failure (rupture at the side of the channel). The average maximum pressurization of fiber-reinforced actuators was between 2.5–3.25 bar, on par with that of

existing elastomer-based micro- [18, 23] and centimeter-scale pneumatic actuators [49]. This range of maximum pressure is approximately 3–12 times higher than recently proposed PDMS actuators fabricated using 3D printing (0.95 bar) [11], soft lithography (0.25 bar) [4], spin coating (1 bar) [20], and inverse-flow injection (1 bar) [50]. Collectively, these results indicate that by modulating the position and orientation of nanofiber sheets, we can both conserve and modulate the curvature of elastomeric micro-actuators while extending the pressurization range.

3.3. Composite structure influences bulk mechanical properties

On the macro- and mesoscale, it is well known that incorporating comparatively stiffer reinforcement fibers in a compliant matrix increases bulk strength and toughness by transferring tensile load from the matrix to the reinforcement material [26, 51–53]. We expected to observe a similar trend by reinforcing micro-scale PDMS actuators with nanofiber sheets. To understand the effect of laminate design and fiber orientation on device mechanics, tensile properties of composite and PDMS-only actuators were quantified using Instron uniaxial testing (supplementary figure 1(b)).

Both three- and four-layer actuators reinforced by parallel nanofibers displayed higher toughness (figure 7(a)), specific ultimate tensile strength (figure 7(b)), and specific elastic modulus (figure 7(c)) than pure PDMS. This increased stiffness explains, in part, the lesser curvature of composite

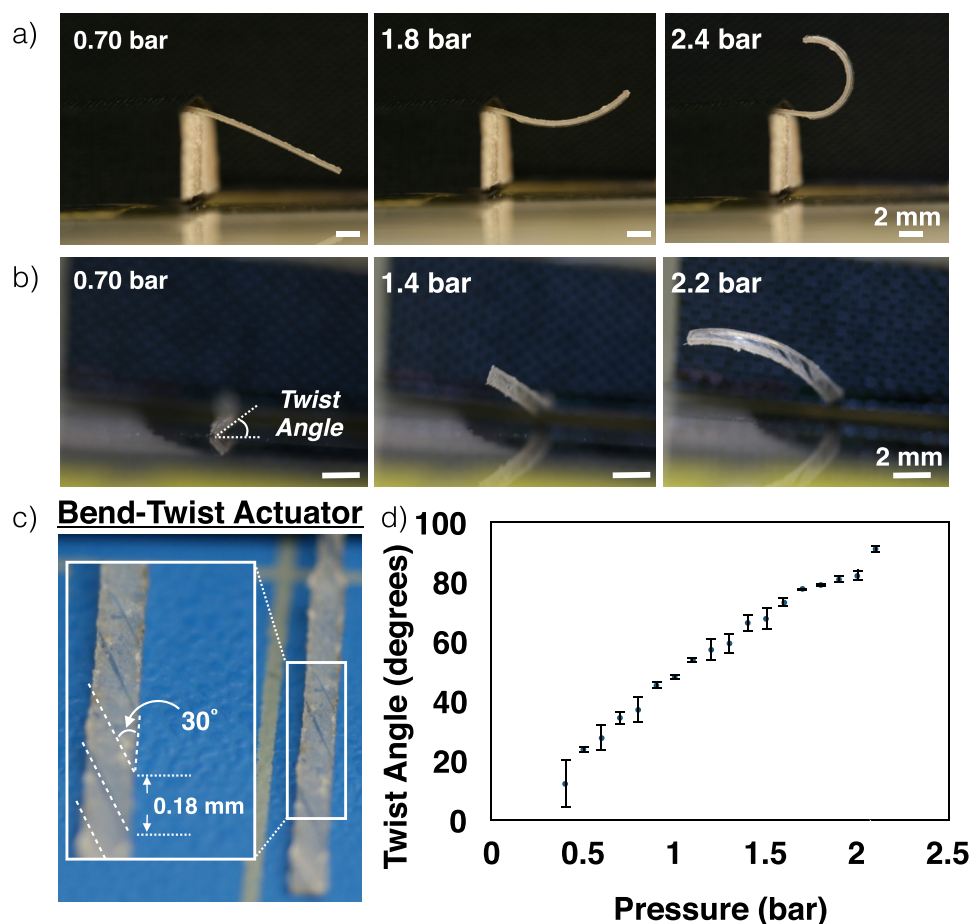


Figure 8. Composite micro-actuators exhibiting (a) pure bending, and (b) bend-twist coupling. (c) Laser-inscribed pattern of bend-twist actuator. (d) Twist angle as a function of pressure. Error reported as SEM. $n = 2$ actuators.

actuators relative to PDMS-only devices. However, three-layer actuators were significantly tougher and stronger than four-layer actuators with fibers in the same respective configurations. Furthermore, unlike four-layer constructs, three-layer laminate devices maintained the elongation of pure PDMS (figure 7(d)). Lastly, a three-layer design with 0° nanofibers displayed a similar toughness to that of a pure nanofiber sheet of the same orientation; this value was 2.3 times greater than the toughness of PDMS alone. Taken as a whole, this data indicates that a three-layer actuator design increases toughness while preserving desired extensibility of elastomer actuators. Based on these results, the three-layer composite design was selected for use in future devices. Examination of samples under a scanning electron microscope revealed no deformation between the nanofiber sheet and PDMS matrix (supplementary figures 1(c) and (d)). As the composite sheet was extended to failure, cracks formed normal to the tensile stress plane and fracture occurred in the plane of fiber fracture. This failure mode is consistent with a reinforcing material that is stronger and more brittle than the matrix material, and with the lack of fiber de-bonding from the surrounding PDMS [54]. It is also possible that the high surface area of nanofibers resists de-bonding of the fiber layer from the surrounding matrix.

3.4. Regulating actuator bending using nanofiber orientation

After demonstrating that nanofiber-reinforced composite actuators bend controllably under pneumatic pressurization (figure 8(a)), we investigated whether varying fiber patterns could be used to achieve more complex bending modes. One mode of interest is the combination of bending and twisting. Prior studies on macro-scale fiber-reinforced actuators have demonstrated that the twisting motion of a pneumatic actuator depends upon fiber orientation [24, 25, 55]. Similarly, Finio *et al* demonstrated that the maximum twist of a piezoelectric micro-actuator occurred when the anisotropic fibrous laminate was oriented at 45° ; zero twist and torque were present at 0° or 90° [56]. Embedding monolithic fiber sheets oriented between 0° and 90° did not induce a twisting mode in composite micro-actuators. We hypothesized that the anisotropy of these sheets was too low to measure a twist. Thus, we predicted that incising a linear pattern onto a uniform nanotextile would induce a bending-twisting mode by reducing cross-coupling in the nonwoven fiber sheet, thereby amplifying anisotropy. To test this hypothesis, we fabricated a composite micro-actuator capable of bend-twist coupling by laser micromachining a pattern of parallel lines on the enclosed nanofiber sheet (figure 8(b)). This approach was

selected because laser cutting provided consistent control of line spacing and pattern uniformity.

Using a custom DPSS laser, lines spaced 0.18 mm apart were inscribed on a monolithic nanofiber sheet (figure 8(c)). A three-layer actuator was prepared using the soft lithography process described in section 2.2. The sub-laminate containing the laser-cut fiber sheet was plasma bonded to the patterned layer at an angle of 30° from the longitudinal axis of the air channel. Although a 30° angle was chosen as a demonstration in this study, further optimization will be the subject of future exploration. The twist angle of bend-twist coupled composite actuators as a function of pressure is shown in figure 8(d) (device was not tested to failure). This preliminary study suggests the potential for using laser patterning to combine multiple actuation modes on the micro-scale. Future studies will build upon this principle to generate multiple curvatures in a single actuator by varying fiber orientation.

4. Conclusion

We have developed a nanofiber-reinforced soft micro-actuator using a novel manufacturing process combining soft lithography and rotary jet spinning. To our knowledge, this is the first study of polymer nanofibers as a strain-limiting layer for micro-actuation. Our results indicate that the mechanical properties and curvature of composite micro-actuators are impacted by nanofiber layer location and bulk fiber orientation. Three-layer fiber-reinforced devices were 2.3 times tougher than pure PDMS, while simultaneously preserving the elongation of the elastomer. Although composite actuators can be pressurized up to 30% higher than pure PDMS devices, no delamination is observed between the strain limiting nanofiber sheet and the PDMS matrix. Finally, by incising an angled pattern into monolithic nanofiber sheets, bend-twist coupling can be achieved for three-layer actuators. Future work will focus on improving analytical modeling to account for varying membrane elasticity throughout inflation, and to capture variations in nanofiber orientation by expanding our laminate plate theory model. These results, in tandem with the customizability of nanofiber-reinforced micro-actuators, will enable more precise control of composite actuator motion. This concept can be extended past cantilevered beams to composite sheets or plates that can be designed to fold into three-dimensional shapes by regulating fiber orientation and air channel position. Thus, nanofiber-reinforced soft fluidic actuators can be leveraged across a variety of applications, including manipulating tissue, interfacing with surgical tools, operating in confined domains, and grasping fragile objects.

Acknowledgments

This work was performed in part at Harvard University's Center for Nanoscale Systems (CNS), a member of the National Nanotechnology Coordinated Infrastructure Network (NNCI), which is supported by the National Science Foundation under

NSF award no. 1541959. Research reported in this publication was supported by the Harvard University Materials Research Science and Engineering Center (MRSEC), NSF Award no. DMR-1420570. The authors gratefully acknowledge helpful comments and feedback from Dr Sheila Russo and Fionnuala Connolly.

ORCID iDs

N R Sinatra  <https://orcid.org/0000-0003-1608-9161>

T Ranzani  <https://orcid.org/0000-0001-8362-3710>

K K Parker  <https://orcid.org/0000-0002-5968-7535>

References

- [1] Rus D and Tolley M T 2015 Design, fabrication and control of soft robots *Nature* **521** 467
- [2] De Volder M and Reynaerts D 2010 Pneumatic and hydraulic microactuators: a review *J. Micromech. Microeng.* **20** 043001
- [3] Laschi C, Mazzolai B and Cianchetti M 2016 Soft robotics: technologies and systems pushing the boundaries of robot abilities *Sci. Robot.* **1** eaah3690
- [4] Martinez R V, Branch J L, Fish C R, Jin L, Shepherd R F, Nunes R, Suo Z and Whitesides G M 2013 Robotic tentacles with three-dimensional mobility based on flexible elastomers *Adv. Mater.* **25** 205–12
- [5] Polygerinos P, Correll N, Morin S A, Mosadegh B, Onal C D, Petersen K, Cianchetti M, Tolley M T and Shepherd R F 2017 Soft robotics: review of fluid-driven intrinsically soft devices; manufacturing, sensing, control, and applications in human-robot interaction *Adv. Eng. Mater.* **19** 1700016
- [6] Russo S, Ranzani T, Walsh C J and Wood R J 2017 An additive millimeter-scale fabrication method for soft biocompatible actuators and sensors *Adv. Mater. Technol.* **2** 1700135
- [7] Hubschman J, Bourges J, Choi W, Mozayan A, Tsirbas A, Kim C and Schwartz S 2010 The microhand: a new concept of micro-forceps for ocular robotic surgery *Eye* **24** 364
- [8] Konishi S, Shimomura S, Tajima S and Tabata Y 2016 Implementation of soft microfingers for a hMSC aggregate manipulation system *Microsyst. Nanoeng.* **2** 15048
- [9] Watanabe Y, Maeda M, Yaji N, Nakamura R and Konishi S 2007 Small, soft, and safe microactuator for retinal pigment epithelium transplantation *IEEE 20th Int. Conf. on Micro Electro Mechanical Systems (IEEE)* pp 659–62
- [10] Sonar H A and Paik J 2016 Soft pneumatic actuator skin with piezoelectric sensors for vibrotactile feedback *Frontiers Robot. AI* **2** 38
- [11] Hwang Y, Paydar O H and Candler R N 2015 Pneumatic microfinger with balloon fins for linear motion using 3D printed molds *Sensors Actuators A* **234** 65–71
- [12] Wakimoto S, Suzumori K and Ogura K 2011 Miniature pneumatic curling rubber actuator generating bidirectional motion with one air-supply tube *Adv. Robot.* **25** 1311–30
- [13] Paek J, Cho I and Kim J 2015 Microrobotic tentacles with spiral bending capability based on shape-engineered elastomeric microtubes *Sci. Rep.* **5** 10768
- [14] Guo H, Zhang J, Wang T, Li Y, Hong J and Li Y 2017 Design and control of an inchworm-inspired soft robot with omega-arching locomotion *IEEE Int. Conf. on Robotics and Automation (IEEE)* pp 4154–9
- [15] Taccola S, Greco F, Sinibaldi E, Mondini A, Mazzolai B and Mattoli V 2015 Toward a new generation of electrically controllable hygromorphic soft actuators *Adv. Mater.* **27** 1668–75

- [16] Morales D, Podolsky I, Mailen R W, Shay T, Dickey M D and Velev O D 2016 Ionoprinted multi-responsive hydrogel actuators *Micromachines* **7** 98
- [17] Gorissen B, De Volder M, De Greef A and Reynaerts D 2011 Theoretical and experimental analysis of pneumatic balloon microactuators *Sensors Actuators A* **168** 58–65
- [18] Gorissen B, Van Hoof C, Reynaerts D and De Volder M 2016 SU8 etch mask for patterning PDMS and its application to flexible fluidic microactuators *Microsyst. Nanoeng.* **2** 16045
- [19] Gorissen B, Chishiro T, Shimomura S, Reynaerts D, De Volder M and Konishi S 2014 Flexible pneumatic twisting actuators and their application to tilting micromirrors *Sensors Actuators A* **216** 426–31
- [20] Liang X, Sun Y and Ren H 2017 A flexible fabrication approach toward the shape engineering of microscale soft pneumatic actuators *IEEE Robot. Autom. Lett.* **2** 165–70
- [21] Gorissen B, Vincentie W, Al-Bender F, Reynaerts D and De Volder M 2013 Modeling and bonding-free fabrication of flexible fluidic microactuators with a bending motion *J. Micromech. Microeng.* **23** 045012
- [22] Li B, Du T, Yu B, van der Gucht J and Zhou F 2015 Caterpillar-inspired design and fabrication of a self-walking actuator with anisotropy, gradient, and instant response *Small* **11** 3494–501
- [23] Jeong O C and Konishi S 2006 All PDMS pneumatic microfinger with bidirectional motion and its application *J. Microelectromech. Syst.* **15** 896–903
- [24] Connolly F, Polygerinos P, Walsh C J and Bertoldi K 2015 Mechanical programming of soft actuators by varying fiber angle *Soft Robot.* **2** 26–32
- [25] Galloway K C, Polygerinos P, Walsh C J and Wood R J 2013 Mechanically programmable bend radius for fiber-reinforced soft actuators *16th Int. Conf. on Advanced Robotics* (IEEE) pp 1–6
- [26] Suzumori K, Endo S, Kanda T, Kato N and Suzuki H 2007 A bending pneumatic rubber actuator realizing soft-bodied manta swimming robot *IEEE Int. Conf. on Robotics and Automation* (IEEE) pp 4975–80
- [27] Kurumaya S, Nabae H, Endo G and Suzumori K 2017 Design of thin McKibben muscle and multifilament structure *Sensors Actuators A* **261** 66–74
- [28] Yao J, Bastiaansen C W and Peijs T 2014 High strength and high modulus electrospun nanofibers *Fibers* **2** 158–86
- [29] Huang Z-M, Zhang Y-Z, Kotaki M and Ramakrishna S 2003 A review on polymer nanofibers by electrospinning and their applications in nanocomposites *Compos. Sci. Technol.* **63** 2223–53
- [30] Khorshidi S, Solouk A, Mirzadeh H, Mazinani S, Lagaron J M, Sharifi S and Ramakrishna S 2016 A review of key challenges of electrospun scaffolds for tissue-engineering applications *J. Tissue Eng. Regen. Med.* **10** 715–38
- [31] Capulli A K et al 2017 JetValve: rapid manufacturing of biohybrid scaffolds for biomimetic heart valve replacement *Biomaterials* **133** 229–41
- [32] Wu S, Duan B, Qin X and Butcher J T 2017 Nanofiber structured hydrogel yarns with pH-response capacity and cardiomyocyte-drivability for bio-microactuator application *Acta Biomaterialia* **60** 144–53
- [33] Lima M D, Hussain M W, Spinks G M, Naficy S, Hagenasr D, Bykova J S, Tolly D and Baughman R H 2015 Efficient, absorption-powered artificial muscles based on carbon nanotube hybrid yarns *Small* **11** 3113–8
- [34] Chattopadhyay S, Hatton T A and Rutledge G C 2016 Aerosol filtration using electrospun cellulose acetate fibers *J. Mater. Sci.* **51** 204–17
- [35] Matulevicius J, Kliucininkas L, Prasauskas T, Buivydiene D and Martuzevicius D 2016 The comparative study of aerosol filtration by electrospun polyamide, polyvinyl acetate, polyacrylonitrile and cellulose acetate nanofiber media *J. Aerosol Sci.* **92** 27–37
- [36] Lee M Y, Hong J, Lee E K, Yu H, Kim H, Lee J U, Lee W and Oh J H 2016 Highly flexible organic nanofiber phototransistors fabricated on a textile composite for wearable photosensors *Adv. Funct. Mater.* **26** 1445–53
- [37] Mogera U, Sagade A A, George S J and Kulkarni G U 2014 Ultrafast response humidity sensor using supramolecular nanofibre and its application in monitoring breath humidity and flow *Sci. Rep.* **4** 4103
- [38] Deravi L F et al 2017 Design and fabrication of fibrous nanomaterials using pull spinning *Macromol. Mater. Eng.* **302** 1600404
- [39] Badrossamay M R, McIlwee H A, Goss J A and Parker K K 2010 Nanofiber assembly by rotary jet-spinning *Nano Lett.* **10** 2257–61
- [40] Golecki H M, Yuan H, Glavin C, Potter B, Badrossamay M R, Goss J A, Phillips M D and Parker K K 2014 Effect of solvent evaporation on fiber morphology in rotary jet spinning *Langmuir* **30** 13369–74
- [41] Vimal S K, Ahamad N and Katti D S 2016 A simple method for fabrication of electrospun fibers with controlled degree of alignment having potential for nerve regeneration applications *Mater. Sci. Eng. C* **63** 616–27
- [42] Arras M M, Grasl C, Bergmeister H and Schima H 2012 Electrospinning of aligned fibers with adjustable orientation using auxiliary electrodes *Sci. Technol. Adv. Mater.* **13** 035008
- [43] Moraes C, Chen J-H, Sun Y and Simmons C A 2010 Micro-fabricated arrays for high-throughput screening of cellular response to cyclic substrate deformation *Lab Chip* **10** 227–34
- [44] Liu M, Sun J, Sun Y, Bock C and Chen Q 2009 Thickness-dependent mechanical properties of polydimethylsiloxane membranes *J. Micromech. Microeng.* **19** 035028
- [45] Myers J A 1962 Handbook of equations for mass and area properties of various geometrical shapes *Technical Report Naval Ordnance Test Station China Lake CA*
- [46] Carver, Inc. Autofour/30-12hc 2016 [Online; accessed August 30, 2017] www.carverpress.com/testing-lab
- [47] Mangan R and Destrade M 2015 Gent models for the inflation of spherical balloons *Int. J. Non-Linear Mech.* **68** 52–8
- [48] Kanner L M and Horgan C O 2007 Elastic instabilities for strain-stiffening rubber-like spherical and cylindrical thin shells under inflation *Int. J. Non-Linear Mech.* **42** 204–15
- [49] Mosadegh B, Polygerinos P, Keplinger C, Wennstedt S, Shepherd R F, Gupta U, Shim J, Bertoldi K, Walsh C J and Whitesides G M 2014 Pneumatic networks for soft robotics that actuate rapidly *Adv. Funct. Mater.* **24** 2163–70
- [50] Sun Y, Song S, Liang X and Ren H 2016 A miniature soft robotic manipulator based on novel fabrication methods *IEEE Robot. Autom. Lett.* **1** 617–23
- [51] Huang Y, King D R, Sun T L, Nonoyama T, Kurokawa T, Nakajima T and Gong J P 2017 Energy-dissipative matrices enable synergistic toughening in fiber reinforced soft composites *Adv. Funct. Mater.* **27** 1605350
- [52] Ichinose N, Ishikawa M and Morimoto K 2011 Effect of stress transfer between fiber and matrix on toughness of polymer composite *Polym. Compos.* **32** 1617–24
- [53] Bayley G, Hedenqvist M and Mallon P 2011 Large strain and toughness enhancement of poly (dimethyl siloxane) composite films filled with electrospun polyacrylonitrile-graft-poly (dimethyl siloxane) fibres and multi-walled carbon nanotubes *Polymer* **52** 4061–72
- [54] Chawla K K and Meyers M 1999 *Mechanical Behavior of Materials* (Englewood Cliffs, NJ: Prentice-Hall)
- [55] Polygerinos P, Wang Z, Overvelde J T, Galloway K C, Wood R J, Bertoldi K and Walsh C J 2015 Modeling of soft fiber-reinforced bending actuators *IEEE Trans. Robot.* **31** 778–89
- [56] Finio B M and Wood R J 2011 Optimal energy density piezoelectric twisting actuators *IEEE/RSJ Int. Conf. on Intelligent Robots and Systems* (IEEE) pp 384–9